symmetry

Article

A Continuum Model on the Triboelectrification Behavior of Dielectric Materials Incorporating Flexoelectricity

Haoyang Zhao, Chuwei Wu, Zhuangzhuang He and Chunli Zhang *

Department of Engineering Mechanics, Zhejiang University, Hangzhou 310027, China
* Correspondence: zhangcl01@zju.edu.cn

Abstract

Triboelectrification has garnered extensive research and application attention; however, certain phenomena remain inadequately explained from a continuum mechanics perspective, particularly the influence of contact force on triboelectrification behavior. Against this backdrop, this study proposes a continuum-mechanics-based quantitative analysis model that incorporates flexoelectricity into triboelectrification, offering an alternative approach to the underlying mechanisms. Subsequently, atomic force microscopy (AFM) is employed to conduct experiments on p-type Si, SiO_2 and polyether ether ketone (PEEK). These experiments systematically investigate the influences of contact force and bias voltages on surface potential. Furthermore, both the experimental and numerical simulation results validate the proposed continuum-mechanics-based model to some extent. These findings show how contact force influences triboelectrification through the flexoelectric mechanism, thereby providing a continuum-mechanical understanding of this complex interaction and advancing the field.

Keywords: triboelectrification; flexoelectricity; contact force; continuum model

1. Introduction

Triboelectrification (TE) generally refers to the process of two electroneutral bodies acquiring net electrical charges when brought into contact and then separated, which is one of the most common and fundamental physical phenomena in nature observed 2500 years ago. For a long time, triboelectrification has been recognized as a nuisance and a hazard, primarily due to electrostatic discharge, which can damage sensitive electronics and ignite flammable materials or dust explosions. Benefiting from the pioneering work by Professor Z.L. Wang and his group on the triboelectric nanogenerator (TENG) [1–3], the triboelectrification phenomenon has been widely harnessed in diverse fields, such as mechanical energy harvesting (from surrounding vibration environment and ocean waves) [4,5], self-powered sensors for smart devices and the IoT [6,7], advanced wastewater treatment [8], and TENG-driven catalysis [9,10], among others. Further applications can be found in recent reviews [11–14].

Understanding the fundamental physical mechanisms of triboelectrification is crucial for both its utilization and for preventing damage caused by it. Due to triboelectrification involving complex factors, it is quite challenging to establish an accurate theoretical model [15–17], especially for quantitative charge transfer. Despite this, there also have been several physically reasonable theoretical models such as the work function model [18,19], the surface state model [20,21], and the electron cloud–potential well model [22,23] for revealing the interfacial triboelectric phenomena between solid surfaces.

Academic Editor: Yunqing Tang

Received: 22 May 2026
Revised: 17 June 2026
Accepted: 9 July 2026
Published: 14 July 2026

While these models can successfully provide reasonable physical explanations for charge transfer, they lack quantitative capability from a continuum perspective. More details can be found in the review works [12,16,24].

In practice, for TENG-based sensors and harvesters in operation, contact force (or mechanical interaction) between two objects always inevitably occurs. However, its influence on charge transfer remains poorly understood, particularly from a quantitative perspective. The contact force-dependent property of TENGs has been observed in a few experiments [16,25–28]. For example, it has been found that the mean peak open-circuit voltage of a TENG, made of two different PDMS films, increases from 2.1 V to 4.6 V when the contact force increases from 0.5 N to 2.5 N in Ref. [28]. A theoretical model incorporating elastic deformation and surface roughness was proposed in Ref. [25]. The change in effective contact area is obvious for materials with a relatively lower elastic modulus. In contrast, it is negligible for materials with a high elastic modulus.

Flexoelectricity refers to the phenomenon of an inhomogeneous deformation generating an electric polarization field in any symmetric dielectric materials [29–31]. It has been pointed out that the flexoelectric-induced polarization field can physically serve as the thermodynamic driving factor for triboelectric charge transfer in Refs. [32,33]. In fact, the effect of flexoelectricity on the charge transfer behavior among polymers, oxides, and silicon materials was characterized experimentally using atomic force microscope (AFM) [34,35]. The surface state model incorporating flexoelectricity for describing surface contributions to the flexoelectric response of finite samples has been proposed [36]; however, it is not enough, especially for quantitatively investigating and predicting multi-field coupling behaviors of TENG-based devices.

Motivated by this insight, this study aims to systematically examine how the magnitude of contact force influences triboelectrification charge transfer in dielectric materials. To quantitatively investigate the effect of the contact force magnitude on charge transfer, we present a multi-field coupling model that integrates flexoelectricity and triboelectric charges from a continuum perspective. This continuum-based framework has several advantages for engineering applications. It can quantitatively predict charge transfer under realistic contact geometries and boundary conditions. It is computationally efficient, so simulations can run at practical scales (from micrometers to meters). It naturally includes gradient effects like flexoelectricity, which matters for contacts where strain gradients are significant. And it couples mechanical and electrostatic fields. Together, these features make the proposed continuum model a practical, reliable tool for studying how contact force affects triboelectrification in engineering settings. As representative examples, we study the charge transfer behavior of three typical samples—p-type Si, SiO_2, and polyether ether ketone (PEEK)—using AFM-based experimental characterizations. These three materials are selected because they possess distinctly different electrical properties—semiconducting (p-type Si), insulating (SiO_2), and polymeric (PEEK). The triboelectric characterization experiment by the AFM tip can be ideally divided into two independent processes, as shown in Figure 1a. During the first process of contact electrification without deformation, there appears the electron transfer caused by the effective work-function difference between the materials, denoting the amount of electron transferred as Q_{CE}. Then, in the subsequent elastic contact process, the non-zero contact force inevitably produces the flexoelectric polarization field, driving the transfer of triboelectric charge with an increasing part denoted as Q_{FE}. The work function at the contact interface is regarded as invariant in this stage [37]. From the viewpoint of multi-field coupling continuum theory, the electron transfer Q_{CE} serves as the electrical boundary condition for the elastic contact process. Thus, the total transfer charge can be represented as Q_{TE} = Q_{CE} + Q_{FE}. This model specifically accounts for the charge transfer process between the sample

https://doi.org/10.3390/sym18071191

and the tip in the contact mode of AFM. We experimentally verified the contribution of contact force to triboelectrification charge transfer and validated the proposed model through a theoretical-simulation-experimental comparison specifically for Si, as, to the best of our knowledge, complete flexoelectric coefficients are currently available only for Si among common dielectric materials.

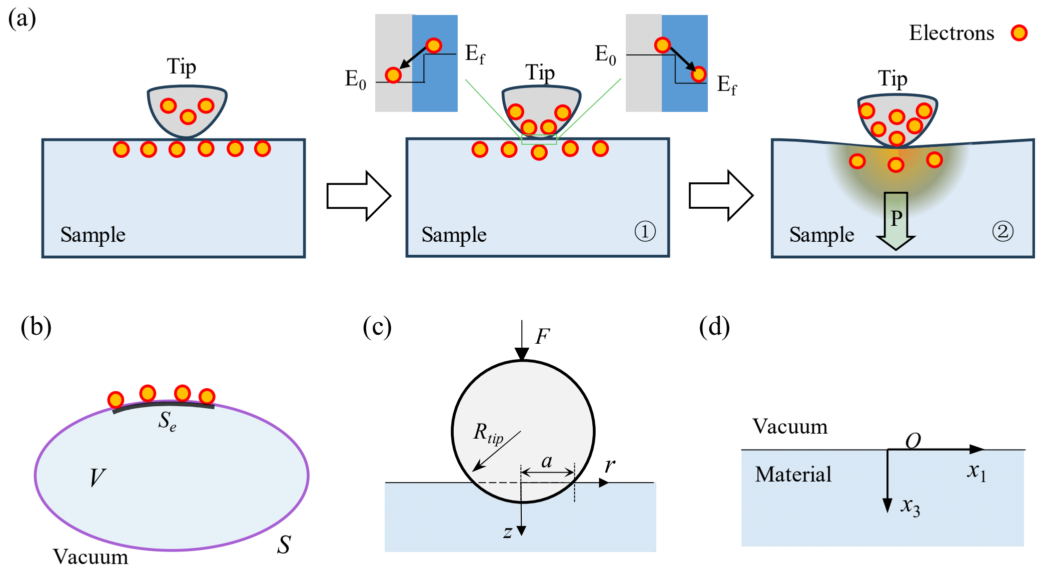

Figure 1. Schematic of physical mechanisms and theoretical models. (**a**) Electron transfer during the process of engagement in AFM experiments: I. Non-contact. II. Contact without deformation. III. Elastic contact. (**b**) Physical boundaries. (**c**) Geometry of Hertzian contact model. (**d**) Reference coordinate system for calculating the electric potential in the p-type Si example.

It should be noted that the total transferred charge considered in the present model contains two physical distinct contributions. The initial contact-electrification charge Q_{CE} (or equivalent surface charge density, σ_{CE}), is generated upon the initial contact of the two materials and serves as the prescribed electrical boundary condition for the subsequent contact process. In contrast, the flexoelectric contribution Q_{FE} is induced by the contact-force-driven strain gradient field, which alters the local polarization and modifies the interfacial potential distribution. Physically, σ_{CE} represents the pre-existing charge state established by contact electrification, while Q_{FE} describes the additional modulation of charge transfer caused by mechanical deformation through flexoelectric coupling. The magnitude and polarity of the initial charge density σ_{CE} depend on several material- and interface-related factors. In particular, the effective work-function difference between the two contacting materials provides the thermodynamic driving force for initial electron transfer. Meanwhile, the electrical conductivity of the contacting bodies affects the charge relaxation and redistribution process after contact. For example, Setiawan and Li [38] demonstrated that tuning the conductivity and work function of a PEDOT: PSS/PEO nanofilm via DMSO addition directly enhanced its adhesive force with Si_3N_4; this enhancement was attributed to the formation of a dipole layer driven by the work-function difference and facilitated by the improved charge mobility, confirming the interplay of these two factors in interfacial charge behavior. In addition, local charge redistribution and the formation of interfacial dipoles may alter the effective interfacial potential barrier, leading to a material-dependent and interface-dependent initial contact-electrification state. These complex microscopic effects are therefore not explicitly resolved but are implicitly embedded into the prescribed value of σ_{CE} adopted in the following continuum model.

2. Continuum Model Incorporating Triboelectricity and Flexoelectricity

Based on the above assumptions concerning contact electrification and charge transfer under elastic deformation, we present a set of fundamental equations that incorporates the coupling of deformation, triboelectricity, and flexoelectricity within a continuum theoretical framework. The developed continuum model can quantitatively describe the influence of contact force magnitude on charge transfer through flexoelectric polarization mechanism.

Consider a dielectric solid occupying domain V with boundary S, and assume the exterior being the vacuum domain V', as shown in Figure 1b. The energy density (W) is written as

$$W = W^L(S_{ij}, P_i, S_{ij,k}) + \frac{1}{2}\varepsilon_0 \varphi_{,i}\varphi_{,i} \tag{1}$$

W^L is the deformation-polarization energy density, which is the function of polarization (P_i), strain (S_{ij}), and strain gradient ($S_{ij,k}$), and reads

$$W^L = \frac{1}{2}a_{ij}P_iP_j + \frac{1}{2}c^p_{ijkl}S_{ij}S_{kl} + f_{ijkl}P_iS_{jk,l} \tag{2}$$

a_{ij}, c^p_{ijkl}, and f_{ijkl} represent the inverse permittivity, elastic and flexoelectric coefficient tensors, respectively. In Equation (1), φ represents the electric potential, ε_0 is the dielectric constant of vacuum. Note that the Cartesian tensor notation and the summation convention are employed, and the indexes of i, j, k, and l take 1, 2, 3, in this work. The electric enthalpy H_e is defined as

$$H_e = W^L - E_iD_i = W^L - \frac{1}{2}\varepsilon_0\varphi_{,i}\varphi_{,i} + \varphi_{,i}P_i \tag{3}$$

E_i and D_i are electric field and electric displacement components, respectively. For the dielectric solid with external electric field E_i^0, traction t_i on the boundary S_t, and charge density σ_{CE} induced by triboelectrification on the boundary S_σ, using the principle of virtual work, there is

$$\int_{V+V'} \delta H_e \mathrm{d}V + \int_V E_i^0 \delta P_i \mathrm{d}V + \int_{S_\sigma} \sigma_{\mathrm{CE}} \delta\varphi \mathrm{d}S + \int_{S_t} t_i \delta u_i \mathrm{d}S = 0 \tag{4}$$

From Equations (2) and (3), the constitutive relations of stress T_{ij}, high-order stress T_{ijk}, and effective local electric field E_i^L can be given as

$$T_{ij} = \frac{\partial W^L}{\partial S_{ij}} = c^p_{ijkl}S_{kl},\ T_{ijk} = \frac{\partial W^L}{\partial S_{ij,k}} = f_{lijk}P_l,\ E_i^L = -\frac{\partial W^L}{\partial P_i} = -(a_{ij}P_j + f_{ijkl}S_{jk,l}) \tag{5}$$

With the help of Equation (5), the governing equations can be obtained by applying the variational operation to Equation (4) as

$$T_{ij,j} - T_{ijk,jk} + f_i = 0,\ E_i^L - \varphi_{,i} + E_i^0 = 0,\ P_{i,i} - \varepsilon_0\varphi_{,ii} = 0,\ \text{in } V \tag{6}$$

and

$$\varphi_{,ii} = 0,\ \text{in } V' \tag{7}$$

along with the corresponding boundary conditions as

$$(T_{ij} - T_{ijk,k})n_j = t_i,\ (\varepsilon_0\varphi_{,i} - P_i)n_i + \sigma_{\mathrm{CE}} = 0 \tag{8}$$

n_i is the direction cosine of the outward normal of boundary. ◎$\varphi_{,i}$◎ represents the jump in the electric field from dielectric domain (V) to vacuum (V'). P_in_i (= σ_{FE}) denotes the polarization charge density induced by flexoelectric polarization at the boundary. The plus or minus sign of σ_{FE} indicates that the flexoelectric effect enhances or offsets the triboelectrification charge density σ_{CE}. So far, we have established the multi-field coupling mechanical model for triboelectricity with elastic deformation, in which the triboelectric charges are treated as an electrical boundary condition. It should be noted that the predictive accuracy of the developed continuum model depends on the accuracy of the input σ_{CE} value, as it serves as the electrical boundary condition in our model.

In practical applications of TENG-based devices, the higher-order stress T_{ijk}, resulting from the polarization-induced deformation by Equations (5) and (6), is a secondary effect and thus negligible. In this case, the force-dependent triboelectric problem can be simplified into a one-way coupled problem for the sake of analytical solution. On the other hand, the tip probe is considered rigid, and its thin alloy layer is neglected in the theoretical analysis, as shown in Figure 1c. This allows the tip probe-sample contact to be treated as a purely elastic process. Its elastic fields can be derived analytically using the classical Hertz contact theory [39,40]. Furthermore, the charges induced by the work-function difference serve as the boundary conditions. Thus, the analytical solutions of electrical quantities can be obtained using Green's function method with reference to the coordinate system defined in Figure 1d, for the center-symmetric silicon under an applied normal concentrated force. See the Supporting Information (D2. Electric fields) for the detailed deriving process.

3. Results and Discussion

In this section, we use AFM to experimentally characterize charge transfer responses of three typical sample materials (i.e., p-type Si, SiO_2 and PEEK) under different tip forces in order to elucidate the underlying mechanism by which contact force influences triboelectrification behavior. The detailed experimental procedures can be found in the Supporting Information (A. Experimental Procedure). We selected a 20 μm × 20 μm area on each of the p-type Si, SiO_2 and PEEK samples for optical scanning; the resulting optical microscope images are shown in Figure 2a–c. Subsequently, a 5 μm × 5 μm region near the center of each scanned area was chosen to characterize triboelectrification behavior in situ. The corresponding three-dimensional surface topography scans are presented in Figure 2d–f. As shown, all three sample surfaces exhibit excellent flatness, which ensures high precision in the subsequent triboelectrification test. Note that for each sample, a relatively flat region is chosen for the AFM/SKPM measurements, and all three samples exhibit negligible piezoelectricity under our experimental conditions [41]; further details are provided in the Supporting Information (B. Exclusion of piezoelectric effect and topographic artifacts [42–46]).

We first perform standard triboelectrification tests without applying a bias voltage on three samples. To ensure elastic contact within reasonable deformation limits and to avoid severe tip/sample damage, the applied contact force ranges were carefully tailored to the specific elastic moduli of each material (e.g., 20–500 nN for the rigid Si and SiO_2, versus 50–900 nN for the softer PEEK). The measured surface potential difference between the tip and the sample surface is shown in Figure 3. It can be seen that the surface potential of p-type Si increases with contact force, whereas that of SiO_2 and PEEK decreases. In addition, the surface potential decays uniformly from the rubbed center outwards, and the altered area is slightly larger than the rubbed area, indicating limited charge diffusion. It should be noted that minor charge variations outside the main rubbed region are attributed to intrinsic surface heterogeneity [47] and fall within the experimental uncertainty of the charge measurements. Therefore, they are treated as background potential variations that do not influence our conclusions.

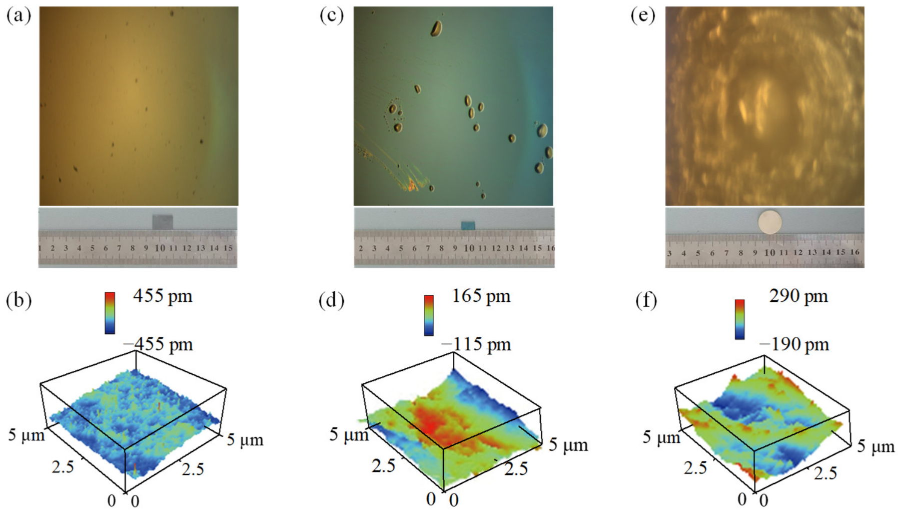

Figure 2. Samples at different scales: (**a**–**c**) the p-type silicon, SiO_2 and PEEK sample surfaces under optical microscopy; (**d**–**f**) three-dimensional topography obtained by AFM scanning.

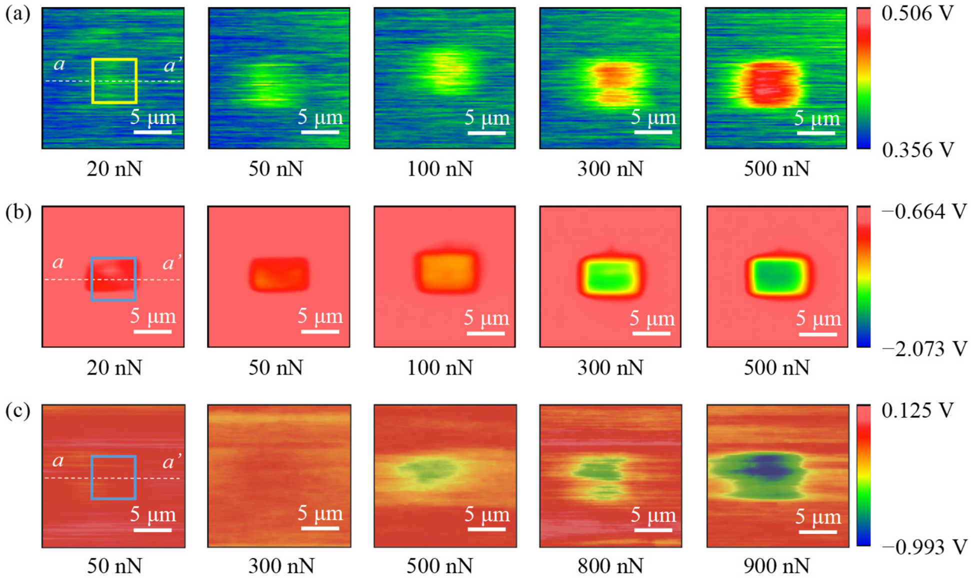

Figure 3. Surface potential rubbed with different contact forces between tip and samples: (**a**) p-type Si, (**b**) SiO_2, and (**c**) PEEK. The yellow and blue squares delineate the rubbed regions, while the white dashed lines indicate the centerlines (a-a') used for extracting surface potential profiles.

Now, for convenience of discussion, we extract the surface potentials (denoted as $V_{a\text{-}a'}$) along the centerline (a-a') of the sample surface, as indicated in Figure 3, and plot them in Figure 4a. As can be seen from Figure 4a, for all three samples, the surface potential within the rubbed region is comparable to that of the surrounding area under low contact forces. However, a significant change in surface potential occurs once the contact force exceeds a critical threshold. In addition, for the p-type Si sample, a downward contact force produces a positive surface potential, whereas it generates negative potential on the SiO_2 and PEEK samples. This behavior is attributed to differences in material properties. As the contact force increases, the absolute value of potential increases accordingly.

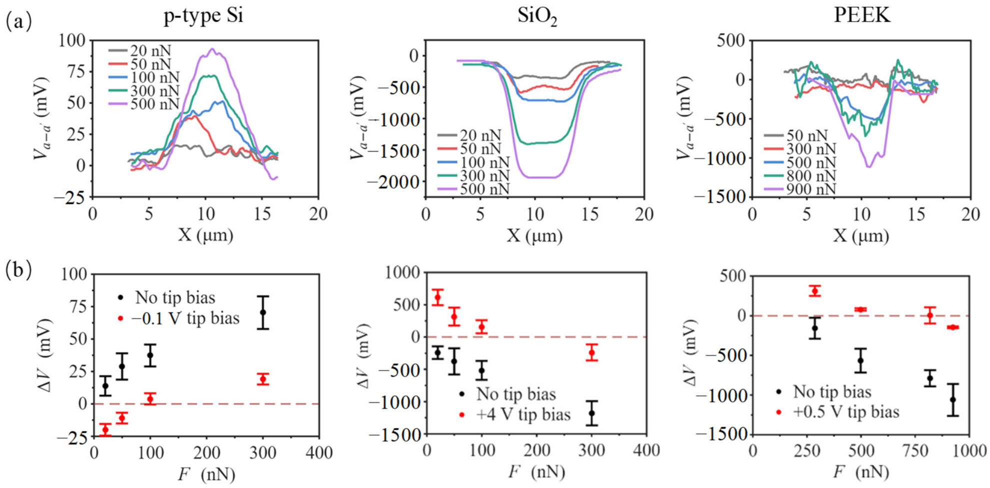

Figure 4. Surface potential for three samples of p-type Si, SiO_2, and PEEK under different conditions. (**a**) Surface potential profiles along line *a-a*′ in the rubbed area for $V_{a\text{-}a'}$. (**b**) Change in surface potential between the rubbed and unrubbed region. Red dots are used to represent conditions where a tip bias voltage is present during rubbing, whereas black dots represent conditions where it is absent.

This observation indicates that changes in contact force lead to variations in the triboelectrification charge transfer behavior. Nevertheless, isolating the specific role of contact force is challenging due to the complexity of the process, which involves multiple interrelated factors such as the accompanying increase in contact area.

To demonstrate the role of the flexoelectric effect in contact force-dependent charge transfer, we apply a tip bias voltage with a polarity opposite to that induced by contact force alone. This bias serves solely as a known electrical reference to highlight the flexoelectric contribution. Based on the results shown in Figure 4a, the tip bias voltages are set to −0.1 V, +4 V, and +0.5 V for the p-type Si, SiO_2, and PEEK samples, respectively. Subsequently, standard triboelectric characterization experiments are conducted on the p−type Si and SiO_2 samples using tip forces of 20, 50, 100, and 300 nN, and on the PEEK sample using tip forces of 300, 500, 800, and 900 nN. The measured surface potential distributions are shown in Figure S4 in the Supporting Information (C. Surface potential distribution under combined contact force and bias voltage).

As shown in Figure S4b–d, under a constant bias, all three samples exhibit a force-dependent reversal of surface potential contrast between the rubbed and non-rubbed regions, which is attributed to the increasing flexoelectric polarization field with tip force. For the p-type Si sample under −0.1 V bias, the surface potential in the rubbed region is lower than that in the non-rubbed region at 20 and 50 nN, but the opposite is true at 100 and 300 nN. For the SiO_2 sample under +4 V bias, the rubbed region shows a higher surface potential at 20–100 nN, with the difference decreasing as contact force increases, and reverses to a lower potential at 300 nN. Similarly, for the PEEK sample under +0.5 V bias, the rubbed region exhibits a higher potential at 300–500 nN, which reverses to a lower potential at 900 nN. These reversals consistently indicate that increasing contact force enhances flexoelectric polarization, thereby altering the surface potential distribution and eventually reversing the charge transfer direction.

To more clearly illustrate this phenomenon and eliminate the influence of background potential, we calculate the difference (ΔV) between the average surface potential in the rubbed region (V_r) and that in the non-rubbed region (V_n) for the above cases. The results are presented in Figure 4b, where ΔV under tip force only is also shown for comparison. Under tip forces alone (20–300 nN), ΔV is positive and increases monotonically from 14.06 mV to 92.27 mV for the p-type Si sample. In contrast, it is negative with increasing magnitude for the SiO_2 sample (from −257.52 mV to −1626.14 mV) and for the PEEK sample (from −82.60 mV to −904.62 mV). Under combined contact force and bias voltage, ΔV reverses the sign with increasing contact force for all three samples (as shown in Figure 4b: for the Si sample, from –19.98 mV (at 20 nN) to 19.02 mV (at 300 nN); for the SiO_2 sample, from 613.246 mV (at 20 nN) to −241.976 mV (at 300 nN); for the PEEK sample, from 313.00 mV (at 300 nN) to −147.22 mV (at 900 nN)). This sign reversal clearly demonstrates that the flexoelectric effect substantially influences triboelectrification charge transfer. Furthermore, it also implies a competitive relationship between the flexoelectric polarization and the bias electric field. Such a phenomenon may be utilized in tribo-engineering applications.

To further validate that flexoelectric polarization plays an important role in triboelectrification charge transfer, we quantitatively investigate the charge transfer behavior under different contact forces using the continuum model established above. We focus here on the p-type Si sample only, because complete flexoelectric coefficient data are unavailable for the other two samples. The material constants of the p-type Si sample used in the calculations are [48]: Young's modulus (E = 190 GPa), Poisson's ratio (ν = 0.26), relative permittivity (ε_r = 11.9), and flexoelectric coefficient (μ_{11} = 0.8928 nC/m; μ_{111}= −0.0927 nC/m; and μ_{14} = 0.4953 nC/m). The p-type Si sample is a rectangular prism with dimensions of 15 mm in length, 30 mm in width, and 500 µm in height. The AFM probe used in the experiment is a sphere-type probe with a tip radius of r_{tip} = 25 nm. With the analytical solutions given in the Supporting Information (D. Analytical solution using Hertz contact model [40,49,50]), the strain gradient fields in the p-type Si sample under different tip forces can be numerically evaluated. Figure 5a shows the strain gradient fields of the p-type Si at the x_1-x_3 plane under a tip force of 20 nN.

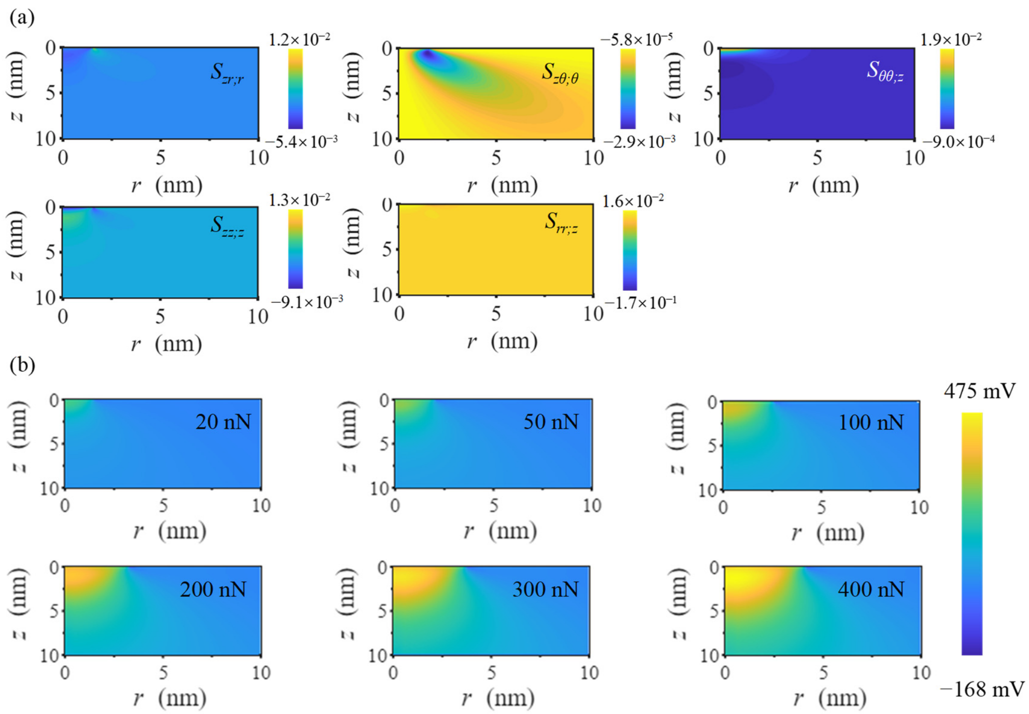

Figure 5. Evaluation with an analytical solution at the x_1-x_3 plane in the p-type Si sample. (**a**) Strain gradient fields under a tip force of 20 nN; (**b**) the flexo–tribo coupled voltages under different tip forces of 20, 50, 100, 200, 300, and 400 nN. The tip probe is located at the reference coordinate system in Figure 1.

The contact-force-induced flexoelectric polarization field and the triboelectrification charges generated at the surface couple together and reach an electrical equilibrium state. This results in an equilibrium distribution of the electrical potential, which can be evalu-

https://doi.org/10.3390/sym18071191

ated with the analytical solution given in the Supporting Information (D2. Electric fields). The surface charge density σ_{CE} for the p-type Si sample is evaluated with the formula $\sigma_{CE} = C_{equ}\, V_{CE}/A$ in the case where no tip forces are present. C_{equ} denotes the equivalent parallel-plate capacitance for the AFM experiment [51]; V_{CE} represents the potential change at zero contact force and is extrapolated from the experimental data. More details are provided in the Supporting Information (E1. Experimental surface potential extraction using the PSF method [51–54]). The value of σ_{CE} is about 23.5 μC/m^2. Figure 5b shows the electrical potential difference relative to the tip probe under varying tip forces of 20, 50, 100, 200, 300, and 400 nN, demonstrating that the rise in the magnitude of the contact force leads to an increase in the electrical field. The surface potential distributions of the sample under different contact forces (20, 50, 100, 200, 300, and 400 nN) are shown in Figure 6a. These results clearly illustrate that increasing contact force simultaneously amplifies the amplitude of the surface-potential variation and enlarges the area over which this perturbation occurs.

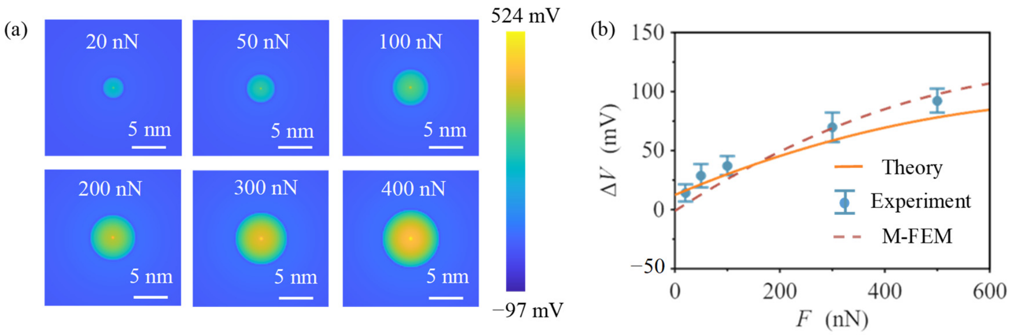

Figure 6. Quantification of contributions of flexoelectricity under different contact forces on p-type Si. (**a**) Theoretical surface potential distribution within the probe contact region. (**b**) Comparison between experiment and calculated ΔV with theoretical model and M-FEM [51].

Comparison between theoretical predictions and experimental results is not feasible because triboelectric characterization experiments using the SKPM mode are performed over a scanned area, whereas theoretical models typically consider point-based interactions. Thus, we analyze the results as follows. For experimental data, ΔV represents the regional average, as discussed previously. For theoretical predictions, we apply the point-spread function (PSF) sampling method [52], based on SKPM principles, to obtain the corresponding potential value V. ΔV is then given by the difference between this value and that of the unrubbed region. The results predicted by the mixed finite element (M-FEM) simulation [55] are also plotted in Figure 6b. Additionally, the proposed theoretical model yields a root mean square error (RMSE) of 11.23 mV and a coefficient of determination (R^2) of 0.88 when compared with the experimental data. Overall, reasonable agreement is achieved among theory, experiment, and simulation. Further details are available in the Supporting Information: E1 (Experimental surface potential extraction using the PSF method) and E2 (Numerical implementation of the analytical solution and M-FEM simulation [56,57]).

4. Conclusions

In summary, this paper develops, from a continuum mechanics perspective, a theoretical model that incorporates the contact-force-induced flexoelectric polarization field and the triboelectrification charges resulting from the work-function difference. This model can be used to quantitatively investigate the effect of contact force magnitude on the triboelectrification charge transfer. Meanwhile, experiments have been conducted on three representative materials (p-type Si, SiO_2 and PEEK) to examine the influence of contact force. The experimental results demonstrate that, despite differences in the magnitude and sign of the surface-potential change, all three representative materials follow a consistent trend as the contact force increases. This indicates that flexoelectricity plays an important role in contact-force-modulated triboelectrification. Moreover, by applying a bias voltage to the probe, we observe a force-driven reversal of the potential change, suggesting that the contact-force modulation of triboelectrification is at least partially mediated by flexoelectricity. This mechanism is further corroborated by analytical derivation and quantitative simulations using M-FEM.

In addition, the present work has several limitations, which can be summarized into four aspects: physical mechanisms, theoretical accuracy, experimental conditions, and general applicability. First, given the complexity of triboelectrification, the present work only accounts for the flexoelectric contribution. The effects of other factors, such as effective contact area influenced by surface flatness [27,58], transfer of materials, ions, or electron transfer, and surface chemical potential, should also be discussed. Second, the origin of the critical contact force threshold is not yet clear. It is probably a combined effect of strain gradients, contact area evolution, and mechanical properties of the materials. Separating out these factors, however, remains a task for future work. Third, the flexoelectric contribution from lateral forces in the experiments is not considered in the present theoretical analysis. Fourth, the current experiments were performed at a constant low scanning speed of 12.5 μm/s. The potential influence of scanning velocity on triboelectrification, though important, has not been examined here and warrants further investigation. Finally, experiments on a broader range of materials are necessary to further verify the accuracy of the proposed continuum-based model. Overall, the main focus of the present work is not to quantitatively predict the material-dependent initial contact-electrification charge Q_{CE} (or surface charge density σ_{CE}), but to reveal how the established contact-electrification state is further modulated by contact-force-induced flexoelectricity. Accordingly, σ_{CE} is treated as a given electrical boundary condition, and the present model emphasizes the subsequent flexoelectric modulation of charge transfer under mechanical contact loading. A quantitative prediction of Q_{CE} or σ_{CE} from first principles, considering work-function difference, conductivity, charge redistribution, surface states, and interfacial dipole formation, remains beyond the scope of this study and will be an important direction for future work.

Supplementary Materials: The following supporting information can be downloaded at: https://www.mdpi.com/article/10.3390/sym18071191/s1, Figure S1. Surface morphologies of the PEEK sample. Figure S2. Piezoelectricity assessment experiment. Figure S3. Exclusion of topographic artifacts of p-type Si under 500 nN. Figure S4. Surface potential rubbed with tip bias voltage between tip and sample. Table S1. Material constants of p-type Si. Table S2. Geometry and load constant.

Author Contributions: Conceptualization, C.Z.; methodology, H.Z., C.W. and C.Z.; validation, C.W. and Z.H.; formal analysis, H.Z.; investigation, H.Z. and C.W.; writing—original draft preparation, H.Z. and C.Z.; writing—review and editing, C.Z.; supervision, C.Z.; project administration, C.Z.; funding acquisition, C.Z. All authors have read and agreed to the published version of the manuscript.

Funding: This research was funded by the National Natural Science Foundation of China (Nos. 12172326) and the Natural Science Foundation of Zhejiang Province (No. LZ25A020007).

Data Availability Statement: The original contributions presented in this study are included in the article/Supplementary Materials. Further inquiries can be directed to the corresponding author.

Acknowledgments: The authors would like to thank the reviewers for their constructive comments that helped improve this manuscript.

Conflicts of Interest: The authors declare no conflicts of interest.

References

1. Xiong, J.Q.; Thangavel, G.; Wang, J.X.; Zhou, X.R.; Lee, P.S. Self-healable sticky porous elastomer for gas-solid interacted power generation. *Sci. Adv.* **2020**, *6*, eabb4246. [CrossRef]
2. Zhao, Z.; Zhou, L.; Li, S.; Liu, D.; Li, Y.; Gao, Y.; Liu, Y.; Dai, Y.; Wang, J.; Wang, Z.L. Selection rules of triboelectric materials for direct-current triboelectric nanogenerator. *Nat. Commun.* **2021**, *12*, 4686. [CrossRef] [PubMed]
3. Nie, J.; Chen, X.; Wang, Z.L. Electrically Responsive Materials and Devices Directly Driven by the High Voltage of Triboelectric Nanogenerators. *Adv. Funct. Mater.* **2018**, *29*, 1806351. [CrossRef]
4. Hao, Y.; Zhou, T.; Gao, X.; Xu, Z.; Zhang, Y.; Zhu, Z.; Wang, Z.L.; Chen, B. Low resonance, omnidirectionally stable triboelectric nanogenerator for ocean wave energy harvesting. *Chem. Eng. J.* **2025**, *526*, 171443. [CrossRef]
5. Zhang, C.; Liu, L.; Zhou, L.; Yin, X.; Wei, X.; Hu, Y.; Liu, Y.; Chen, S.; Wang, J.; Wang, Z.L. Self-Powered Sensor for Quantifying Ocean Surface Water Waves Based on Triboelectric Nanogenerator. *ACS Nano* **2020**, *14*, 7092–7100. [CrossRef] [PubMed]
6. Zhao, K.; Wang, Z.L.; Yang, Y. Self-Powered Wireless Smart Sensor Node Enabled by an Ultrastable, Highly Efficient, and Superhydrophobic-Surface-Based Triboelectric Nanogenerator. *ACS Nano* **2016**, *10*, 9044–9052. [CrossRef] [PubMed]
7. Wang, Z.; Wu, Y.; Jiang, W.; Liu, Q.; Wang, X.; Zhang, J.; Zhou, Z.; Zheng, H.; Wang, Z.; Wang, Z.L. A Universal Power Management Strategy Based on Novel Sound-Driven Triboelectric Nanogenerator and Its Fully Self-Powered Wireless System Applications. *Adv. Funct. Mater.* **2021**, *31*, 2103081. [CrossRef]
8. Chen, S.; Wang, N.; Ma, L.; Li, T.; Willander, M.; Jie, Y.; Cao, X.; Wang, Z.L. Triboelectric Nanogenerator for Sustainable Wastewater Treatment via a Self-Powered Electrochemical Process. *Adv. Energy Mater.* **2016**, *6*, 1501778. [CrossRef]
9. Yao, S.; Zhao, X.; Wang, X.; Huang, T.; Ding, Y.; Zhang, J.; Zhang, Z.; Wang, Z.L.; Li, L. Bioinspired Electron Polarization of Nanozymes with a Human Self-Generated Electric Field for Cancer Catalytic Therapy. *Adv. Mater.* **2022**, *34*, 2109568. [CrossRef] [PubMed]
10. Wang, Z.; Dong, X.; Li, X.-F.; Feng, Y.; Li, S.; Tang, W.; Wang, Z.L. A contact-electro-catalysis process for producing reactive oxygen species by ball milling of triboelectric materials. *Nat. Commun.* **2024**, *15*, 757. [CrossRef] [PubMed]
11. Zhou, L.; Liu, D.; Wang, J.; Wang, Z.L. Triboelectric nanogenerators: Fundamental physics and potential applications. *Friction* **2020**, *8*, 481–506. [CrossRef]
12. Wang, Z.L. From contact electrification to triboelectric nanogenerators. *Rep. Prog. Phys.* **2021**, *84*, 096502. [CrossRef] [PubMed]
13. Cheng, T.; Shao, J.; Wang, Z.L. Triboelectric nanogenerators. *Nat. Rev. Methods Prim.* **2023**, *3*, 39. [CrossRef]
14. Fu, X.; Pan, X.; Liu, Y.; Li, J.; Zhang, Z.; Liu, H.; Gao, M. Non-Contact Triboelectric Nanogenerator. *Adv. Funct. Mater.* **2023**, *33*, 2306749. [CrossRef]
15. Pecunia, V.; Silva, S.R.P.; Phillips, J.D.; Artegiani, E.; Romeo, A.; Shim, H.; Park, J.; Kim, J.H.; Yun, J.S.; Welch, G.C.; et al. Roadmap on energy harvesting materials. *J. Phys. Mater.* **2023**, *6*, 0425001. [CrossRef] [PubMed]
16. Wang, Z.L.; Wang, A.C. On the origin of contact-electrification. *Mater. Today* **2019**, *30*, 34–51. [CrossRef]
17. Matsusaka, S.; Maruyama, H.; Matsuyama, T.; Ghadiri, M. Triboelectric charging of powders: A review. *Chem. Eng. Sci.* **2010**, *65*, 5781–5807. [CrossRef]
18. Harper, W.R. The Volta effect as a cause of static electrification. *Proc. R. Soc. London. Ser. A. Math. Phys. Sci.* **1997**, *205*, 83–103. [CrossRef]
19. Davies, D.K. Charge Generation on Dielectric Surfaces. *J. Phys. D. Appl. Phys.* **1969**, *2*, 1533. [CrossRef]
20. Lowell, J. Surface states and the contact electrification of polymers. *J. Phys. D. Appl. Phys.* **1977**, *10*, 65. [CrossRef]
21. Li, S.; Zhou, Y.; Zi, Y.; Zhang, G.; Wang, Z.L. Excluding Contact Electrification in Surface Potential Measurement Using Kelvin Probe Force Microscopy. *ACS Nano* **2016**, *10*, 2528–2535. [CrossRef] [PubMed]
22. Xu, C.; Zi, Y.; Wang, A.C.; Zou, H.; Dai, Y.; He, X.; Wang, P.; Wang, Y.C.; Feng, P.; Li, D.; et al. On the Electron-Transfer Mechanism in the Contact-Electrification Effect. *Adv. Mater.* **2018**, *30*, 1706790. [CrossRef] [PubMed]
23. Xu, C.; Zhang, B.; Wang, A.C.; Zou, H.; Liu, G.; Ding, W.; Wu, C.; Ma, M.; Feng, P.; Lin, Z.; et al. Contact-Electrification between Two Identical Materials: Curvature Effect. *ACS Nano* **2019**, *13*, 2034–2041. [CrossRef] [PubMed]
24. Niu, S.; Wang, Z.L. Theoretical systems of triboelectric nanogenerators. *Nano Energy* **2015**, *14*, 161–192. [CrossRef]
25. Wen, J.; He, H.; Niu, C.; Rong, M.; Huang, Y.; Wu, Y. An improved equivalent capacitance model of the triboelectric nanogenerator incorporating its surface roughness. *Nano Energy* **2022**, *96*, 107070. [CrossRef]
26. Lee, K.Y.; Kim, S.K.; Lee, J.H.; Seol, D.; Gupta, M.K.; Kim, Y.; Kim, S.W. Controllable Charge Transfer by Ferroelectric Polarization Mediated Triboelectricity. *Adv. Funct. Mater.* **2016**, *26*, 3067–3073. [CrossRef]
27. Min, G.; Xu, Y.; Cochran, P.; Gadegaard, N.; Mulvihill, D.M.; Dahiya, R. Origin of the contact force-dependent response of triboelectric nanogenerators. *Nano Energy* **2021**, *83*, 105829. [CrossRef]
28. Kaur, A.; Singh, S.; Jadaun, S.; Gupta, A.; Sapra, G. Impact of deformation on the structural and electronic properties of MWCNT-PDMS based triboelectric nanogenerator. *J. Mater. Sci. Mater. Electron.* **2024**, *35*, 121. [CrossRef]
29. Yudin, P.V.; Tagantsev, A.K. Fundamentals of flexoelectricity in solids. *Nanotechnology* **2013**, *24*, 432001. [CrossRef] [PubMed]
30. Zubko, P.; Catalan, G.; Tagantsev, A.K. Flexoelectric Effect in Solids. *Annu. Rev. Mater. Res.* **2013**, *43*, 387–421. [CrossRef]

31. Majdoub, M.S.; Sharma, P.; Cagin, T. Enhanced size-dependent piezoelectricity and elasticity in nanostructures due to the flexoelectric effect. *Phys. Rev. B* **2008**, *77*, 125424, Erratum in *Phys. Rev. B* **2009**, *79*, 119904.. [CrossRef]
32. Mizzi, C.A.; Marks, L.D. When Flexoelectricity Drives Triboelectricity. *Nano Lett.* **2022**, *22*, 3939–3945. [CrossRef] [PubMed]
33. Mizzi, C.A.; Lin, A.Y.W.; Marks, L.D. Does Flexoelectricity Drive Triboelectricity? *Phys. Rev. Lett.* **2019**, *123*, 116103. [CrossRef] [PubMed]
34. Lin, S.; Zheng, M.; Xu, L.; Zhu, L.; Wang, Z.L. Electron transfer driven by tip-induced flexoelectricity in contact electrification. *J. Phys. D. Appl. Phys.* **2022**, *55*, 315502. [CrossRef]
35. Qiao, H.; Zhao, P.; Kwon, O.; Sohn, A.; Zhuo, F.; Lee, D.M.; Sun, C.; Seol, D.; Lee, D.; Kim, S.W.; et al. Mixed Triboelectric and Flexoelectric Charge Transfer at the Nanoscale. *Adv. Sci.* **2021**, *8*, 2101793. [CrossRef] [PubMed]
36. Mizzi, C.A.; Marks, L.D. The role of surfaces in flexoelectricity. *J. Appl. Phys.* **2021**, *129*, 224102. [CrossRef]
37. Leung, T.C.; Kao, C.L.; Su, W.S.; Feng, Y.J.; Chan, C.T. Relationship between surface dipole, work function and charge transfer: Some exceptions to an established rule. *Phys. Rev. B* **2003**, *68*, 195408. [CrossRef]
38. Setiawan, R.C.; Li, D.Y. Tuning the conductivity and electron work function of a spin-coated pedot:pss/peo nanofilm for enhanced interfacial adhesion. *Langmuir* **2021**, *37*, 4924–4932. [CrossRef] [PubMed]
39. Johnson, K.L. *Contact Mechanics*; Cambridge University Press: Cambridge, UK, 1985.
40. Huber, M.T. Zur Theorie der Berührung fester elastischer Körper. *Ann. Phys.* **2006**, *319*, 153–163. [CrossRef]
41. Scott, J.F. Soft-mode spectroscopy: Experimental studies of structural phase transitions. *Rev. Mod. Phys.* **1974**, *46*, 83–128. [CrossRef]
42. Choi, S.B.; Veeralingam, S.; Khanh, T.D.; Choi, J.S.; Kishore, K.R.; Jung, S.-B.; Kim, J.-W. Rapid-response hybrid piezo-triboelectric pressure sensor using all-fabric materials for enhanced sensing and power generation. *Nano Energy* **2025**, *140*, 111000. [CrossRef]
43. Li, F.; Jin, L.; Xu, Z.; Zhang, S. Electrostrictive effect in ferroelectrics: An alternative approach to improve piezoelectricity. *Appl. Phys. Rev.* **2014**, *1*, 011103. [CrossRef]
44. Mason, W.P.; Baerwald, H. Piezoelectric Crystals and Their Applications to Ultrasonics. *Phys. Today* **1951**, *4*, 23–24. [CrossRef]
45. Lu, X.; Qu, H.; Skorobogatiy, M. Piezoelectric Micro- and Nanostructured Fibers Fabricated from Thermoplastic Nanocomposites Using a Fiber Drawing Technique: Comparative Study and Potential Applications. *ACS Nano* **2017**, *11*, 2103–2114. [CrossRef] [PubMed]
46. Joo, S.; Eom, S.; Choi, Y.; Jeong, U.; Cho, Y.; Yu, W.; Park, K.; Hong, S. Atomic Force Microscopy for Cross-Disciplinary Materials Research. *Small Methods* **2025**, *9*, 2017. [CrossRef] [PubMed]
47. Cunningham, R.G.; Montgomery, D.J. Studies in the Static Electrification of Filaments. *Text. Res. J.* **1958**, *28*, 971–979. [CrossRef]
48. Sun, L.; Zhu, L.; Zhang, C.; Chen, W.; Wang, Z. Mechanical Manipulation of Silicon-based Schottky Diodes via Flexoelectricity. *Nano Energy* **2021**, *83*, 105855. [CrossRef]
49. Mindlin, R.D. Polarization gradient in elastic dielectrics. *Int. J. Solids Struct.* **1968**, *4*, 637–642. [CrossRef]
50. Popov, V.L.; Heß, M.; Willert, E. *Handbook of Contact Mechanics: Exact Solutions of Axisymmetric Contact Problems*; Springer: Berlin/Heidelberg, Germany, 2019.
51. Koley, G.; Spencer, M.G.; Bhangale, H.R. Cantilever effects on the measurement of electrostatic potentials by scanning Kelvin probe microscopy. *Appl. Phys. Lett.* **2001**, *79*, 545–547. [CrossRef]
52. Lenton, I.C.D.; Pertl, F.; Shafeek, L.; Waitukaitis, S.R. Beyond the blur: Using experimentally determined point spread functions to improve scanning Kelvin probe imaging. *J. Appl. Phys.* **2024**, *136*, 045305. [CrossRef]
53. Giessibl, F.J. Advances in atomic force microscopy. *Rev. Mod. Phys.* **2003**, *75*, 949–983. [CrossRef]
54. Lenton, I.C.D.; Pertl, F.; Shafeek, L.; Waitukaitis, S.R. A Duality Between Surface Charge and Work Function in Scanning Kelvin Probe Microscopy. *Adv. Mater. Interfaces* **2025**, *12*, e00521. [CrossRef]
55. He, Z.Z.; Zhao, H.Y.; Kong, Y.F.; Zhang, W.S.; Zhang, C.L.; Chen, W.Q. An efficient model for coupled flexoelectric plate-RLC circuit system. *Int. J. Mech. Sci.* **2025**, *304*, 110716. [CrossRef]
56. He, Z.Z.; Zhao, H.Y.; Zhou, Y.C.; Xu, B.X.; Chen, W.Q.; Zhang, C.L. An efficient and accurate beam-type M-FEM incorporating flexoelectricity and external RLC circuits. *Thin-Walled Struct.* **2025**, *216*, 113648. [CrossRef]
57. He, Z.Z.; Zhang, C.L.; Zhang, C.Z.; Chen, W.Q. Programmable dielectric metamaterial plates via flexoelectricity and L-C circuits. *Int. J. Mech. Sci.* **2025**, *286*, 109937. [CrossRef]
58. Wang, Q.; Wang, T.; Liu, Y.; Xie, S.; Du, S.; Li, Y.; Yu, J.; Zhang, L.; Li, D.; Li, D.; et al. 3D visualization microscope of TENG contact interface based on astigmatic imaging. *Nano Energy* **2024**, *129*, 110061. [CrossRef]